Multifunctional Biocomposite Materials from *Chlorella vulgaris* Microalgae

Israel Kellersztein,* Daniel Tish, John Pederson, Martin Bechthold, and Chiara Daraio*

Extrusion 3D-printing of biopolymers and natural fiber-based biocomposites enables the fabrication of complex structures, ranging from implants' scaffolds to eco-friendly structural materials. However, conventional polymer extrusion requires high energy consumption to reduce viscosity, and natural fiber reinforcement often requires harsh chemical treatments to improve adhesion. We address these challenges by introducing a sustainable framework to fabricate natural biocomposites using *Chlorella vulgaris* microalgae as the matrix. Through bioink optimization and process refinement, we produced lightweight, multifunctional materials with hierarchical architectures. Infrared spectroscopy analysis reveals that hydrogen bonding plays a critical role in the binding and reinforcement of *Chlorella* cells by hydroxyethyl cellulose (HEC). As water content decreases, the hydrogen bonding network evolves from water-mediated interactions to direct hydrogen bonds between HEC and *Chlorella*, enhancing the mechanical properties. A controlled dehydration process maintains continuous microalgae morphology, preventing cracking. The resulting biocomposites exhibit a bending stiffness of 1.6 GPa and isotropic heat transfer and thermal conductivity of 0.10 W/mK at room temperature, demonstrating effective thermal insulation. These characteristics make *Chlorella* biocomposites promising candidates for applications requiring both structural performance and thermal insulation, offering a sustainable alternative to conventional materials in response to growing environmental demands.

1. Introduction

3D printing is a versatile processing method that facilitates the fabrication of biocomposites and biopolymers by enabling the production of intricate geometries and customized designs with precise control over material deposition.[1,2] Extrusion 3D printing, which accommodates a wide range of biopolymer compositions, has been widely used in various fields including healthcare[3,4] and structural applications.[5,6] Biomaterials used in tissue regeneration[7,8] or environmental applications,[9,10] for instance, are often gel-based, capable of delivering nutrients effectively to targeted cells and promoting cell proliferation.[7,11,12] These gels often exhibit soft mechanical properties, with Young's modulus values typically in the range of $\approx$1–200 kPa, contingent on the cross-linking density of the printed gels and reinforcement components.[13,14] Fabricating scaffolds via 3D printing can involve the use of stiffer materials, such as poly(lactic acid) and polycaprolactone, with mechanical properties tailored to match the stiffness of the target tissue for regeneration, e.g., bone, reaching a Young's modulus ranging from 40 MPa to 1 GPa.[15–17]

Polymer biocomposites for structural applications, typically composed of a polymer matrix reinforced with wood or natural fibers, are intended to withstand larger stresses, necessitating higher stiffness. Similar to conventional processing methods like injection molding or extrusion, 3D printing these biocomposites involves significant fabrication challenges. The polymer matrices often exhibit high viscosities, complicating conventional extrusion 3D printing unless high temperatures are involved, resulting in high energy consumption.[18,19] Moreover, optimizing the interaction between the matrix and the reinforcement materials requires meticulous treatments to enhance stress transfer efficiency.[20–22]

Microalgae present a promising avenue for addressing environmental challenges. These unicellular, aquatic microorganisms are widely distributed and capable of thriving in diverse environments, including seawater, freshwater, and bioreactors. Their ability to adapt to various growth conditions minimizes competition with conventional crops that require specific environments, while efficiently performing photosynthesis to convert carbon dioxide into oxygen.[23–25] Microalgae, with their diverse composition of proteins, lipids, and polysaccharide, as well as their unique cell morphology, have become central to sustainable research across various applications, including biofuels,

I. Kellersztein, J. Pederson, C. Daraio
Division of Engineering and Applied Science
California Institute of Technology
Pasadena, CA 91125, USA
E-mail: israelke@caltech.edu; daraio@caltech.edu
I. Kellersztein
Resnick Sustainability Institute
California Institute of Technology
Pasadena, CA 91125, USA
D. Tish, M. Bechthold
Material Processes and Systems Group
Graduate School of Design
Harvard University
Cambridge, MA 02138, USA

**ADVANCED
SCIENCE NEWS**

www.advancedsciencenews.com

**ADVANCED
MATERIALS**

www.advmat.de

food additives, cosmetics, and wastewater purification.[26] Recent advancements in materials science and engineering have demonstrated the use of microalgae biomass as a natural polymer source for bioplastic synthesis.[27,28] Additionally, microalgae have been explored as fillers in polymer blends,[29,30] composites,[31,32] and cement[33] through conventional fabrication processes, such as compounding followed by injection molding,[31] compression molding,[30,32] and solvent casting.[29] These studies report a decrease in the mechanical properties of the blends and biocomposites with increasing microalgae concentration, for example, *Chlorella* reduced the strength and stiffness of polyethylene by 60% and 50%, respectively, whereas the strength and stiffness of poly(lactic acid) were reduced by 61% and 40%, respectively, when introducing microalgae into the material composition.[29–32] Additionally, research indicates that adding microalgae to cement reduces the matrix strength by up to ≈80%.[33]

Recent studies have focused on adapting microalgae for extrusion 3D printing, offering a sustainable and renewable material source.[34,35] 3D printing with microalgae presents a more sustainable alternative to conventional processing methods, such as printing at room temperature and using water as a solvent to control bioink rheology. *C. vulgaris* microalgae suspensions, with varying particle volume fractions (up to 60 vol%), were produced and nonpolar oils were incorporated into the suspensions to minimize macroscopic defects in printed structures postdehydration. Although the mechanical properties of the printed *Chlorella*-based materials were not investigated, the evaporation of water and oil during dehydration introduced defects within the materials' microstructure,[34] likely impacting the mechanical properties. In a subsequent study, the reinforcement effect of cellulose fibers and drying methods, such as freeze-drying, oven drying, and desiccator, on the mechanical properties of 3D printed *Spirulina* biocomposites was investigated.[35] At the macroscale, they observed that freeze-drying the materials maintained their integrity, while oven and desiccator drying caused cracks and deformation.[35] At the microscale, they reported that oven and desiccator drying introduced microcracks, while freeze-drying resulted in a foam-like structure from solvent evaporation.[35] Cellulose fibers were required to deliver a strong material, with a large concentration (20 wt%) of fibers leading to a compression strength of 16.4 MPa, though the modulus did not exhibit a similar improvement trend.[35] All these prior studies demonstrate that 3D printing offers flexibility in designing structures and achieving complex geometrical shapes,[36] however, controlling post-printing processes, such as dehydration of natural-based bioink, is crucial for maximizing the mechanical functionality of the material.

Building on previous studies,[34,35] we improve fabrication approaches and post-printing processes to obtain lightweight, hierarchical *Chlorella*-based biocomposite materials using extrusion 3D printing at room temperature and without the introduction of any petrochemical components (**Figure 1**). Our approach optimizes the composition of the bioink, which is a biomaterial-based ink used in bioprinting. We also employ a controlled material dehydration process to produce biocomposite materials with enhanced mechanical and thermal properties. We control the rheology of the slurries to improve ink flow and overall printability. We detail the role of processing parameters and reinforcement

concentration on the mechanical and thermal properties of the *Chlorella* biocomposites. Our approach is adaptable to other microalgae systems, enabling the fabrication of intricate 3D structures on a large scale.

2. Results and Discussion

We studied multiple printing and dehydration parameters, to maximize the materials' properties of the printed biocomposites. This included a detailed characterization of the bioink rheology and selection of the ink's composition, to improve printability (**Figure 2A–H**). After fabrication and dehydration, we performed structural (Figure 2I–M), mechanical (**Figure 3A–L**), and thermal analyses (**Figure 4A–D**) of the final biocomposites. The parameters' selection followed an iterative process that evaluated the role of each variable as a function of all the others (see the Experimental Section in the Supporting Information for the description of the tests performed).

2.1. Bioink Composition and 3D Printing of Biocomposites

The bioinks used in our work were formulated to minimize the embodied carbon and include no petrochemical compounds. Additionally, the bioinks were printed at room temperature and printing patterns were shaped precisely to reduce the processing waste (refer to the Experimental Section in the Supporting Information).

The bioink composition integrates *C. vulgaris* cells that have a spherical shape and are reported to have diameters ranging from 2 to 10 μm.[37] We used ultrapure *Chlorella* with a cell diameter of 3.21 ± 0.21 μm in its dry state (Figure S1, Supporting Information). These specific microalgae were grown in glass tubes, diminishing the presence of additional components, or impurities, which may interact weakly with *Chlorella* cells, resulting in discontinuities and defects that could affect the final properties of the biocomposite material. *C. vulgaris* was selected for the present study due to its suitability for direct ink writing, a form of extrusion 3D printing. Its small cell size facilitates smooth extrusion and precise deposition, ensuring good printability. Additionally, the cell walls of *Chlorella* are rich in cellulose, which is expected to serve as a natural reinforcing agent to enhance the mechanical properties of the biocomposites.[38] The industrial availability of *C. vulgaris* further supports its use as a sustainable and scalable resource for biocomposite production.

Microalgae-based biocomposites were fabricated via 3D printing using viscous suspensions of *Chlorella* dispersed in water with 2-hydroxyethyl cellulose (HEC). The process involves initially dispersing HEC in water, followed by the incorporation of microalgal cells into the mixture (Figure 1I). HEC was integrated into the bioink to fulfill two objectives: i) as a binder, enhancing cell immobilization through gelation;[39] ii) as the reinforcement component in the biocomposite, as HEC can create strong physical interactions, such as hydrogen bonding, with the *Chlorella* cells.[40] The bioink was printed into mechanically stable hierarchical structures of cubic ($20 \times 20 \times 10$ mm³) and rectangular ($70l \times 13w \times 4t$ mm³) shapes (Figure 1II–IV).

Cellulose ethers and esters are commonly used in 3D bioprinting as thickeners and binders due to their water solubility, which

ADVANCED
SCIENCE NEWS
www.advancedsciencenews.com
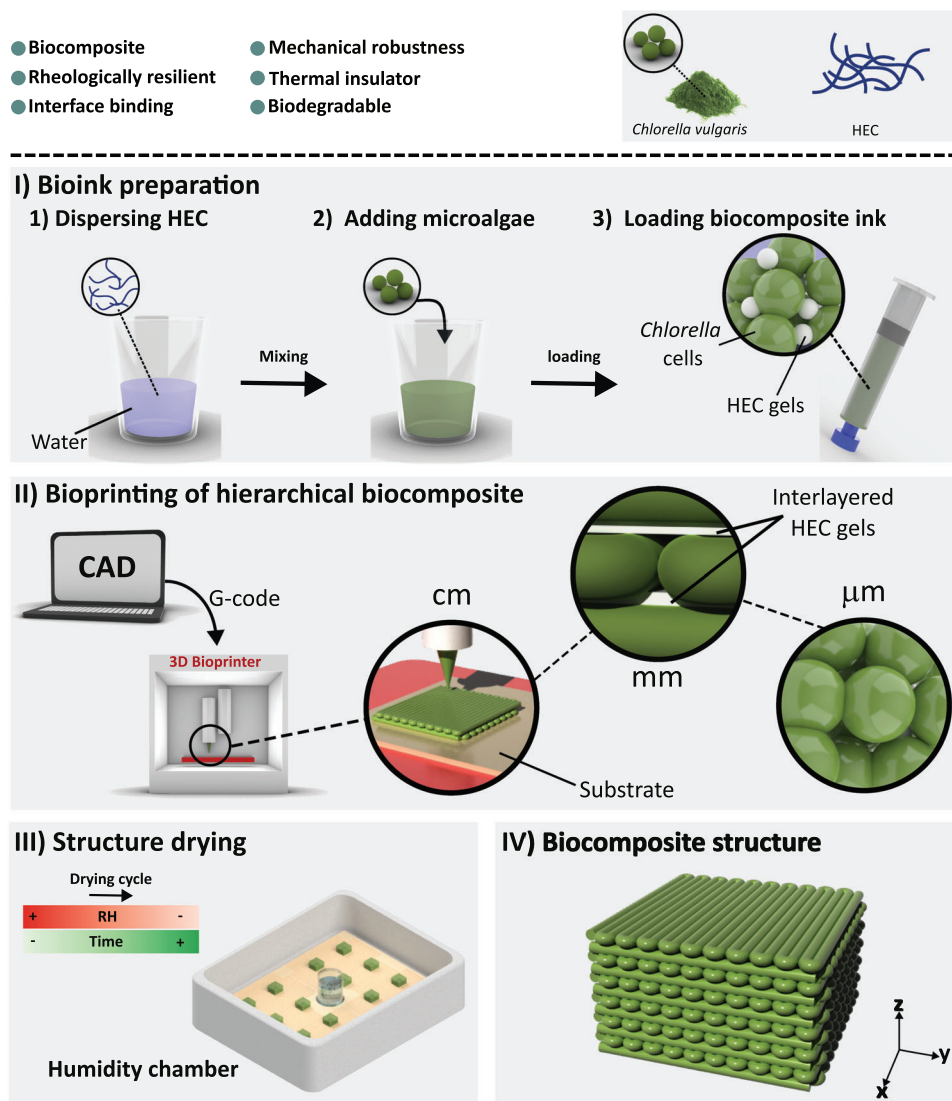
ADVANCED
MATERIALS
www.advmat.de

Figure 1. Schematic diagram of the fabrication processes used in *C. vulgaris* biocomposites. The top row lists the properties and components used. I–IV) The steps for the fabrication of *Chlorella* biocomposites, highlighting the micro-, milli-, and centimeter length scales within the material's hierarchical structure. The final samples fabricated are $20 \times 20 \times 10$ mm^3.

facilitates their integration into bioink formulations.[39] In this study, HEC was selected for its ability to gel at room temperature, aligning with our goal of heat-free processing and simplifying fabrication compared to alternatives like methyl cellulose, which require additional thermal steps. Additionally, HEC's higher hydrophilicity and polarity relative to other cellulose derivatives, such as hydroxypropyl cellulose and hydroxypropyl methylcellulose, enables faster swelling and is expected to improve binding interactions with *Chlorella* microalgae.[41,42] These properties can contribute to enhanced cohesion within the biocomposite matrix.

To define the optimal water content in the bioink, we selected an initial HEC concentration of 5 wt%, relative to the biomass concentration (Figure 2A). At water concentrations below 56 wt%, the bioink was too viscous to be printed, while at water concentrations above 66 wt%, the bioink was too fluid to

be precisely deposited using the minimum pressure of the 3D printer. After dehydrating the printed samples using the protocol described in Section 2.3, we observed an inverse relationship between volumetric shrinkage and density: higher water concentrations in the bioink led to increased evaporation, causing greater shrinkage and reduced density.

After printing, inconsistencies in sample weight were observed despite using consistent printing conditions (Figure S2a, Supporting Information). These variations, which can affect the density and mechanical properties of the biocomposites, were attributed to the increased viscosity of the *Chlorella*-based bioink over time (Figure S2b,c, Supporting Information). HEC is commonly used as a rheological additive to improve the printability and shape fidelity of bioinks for extrusion 3D printing by increasing viscosity and enhancing flow behavior.[43] This increase in
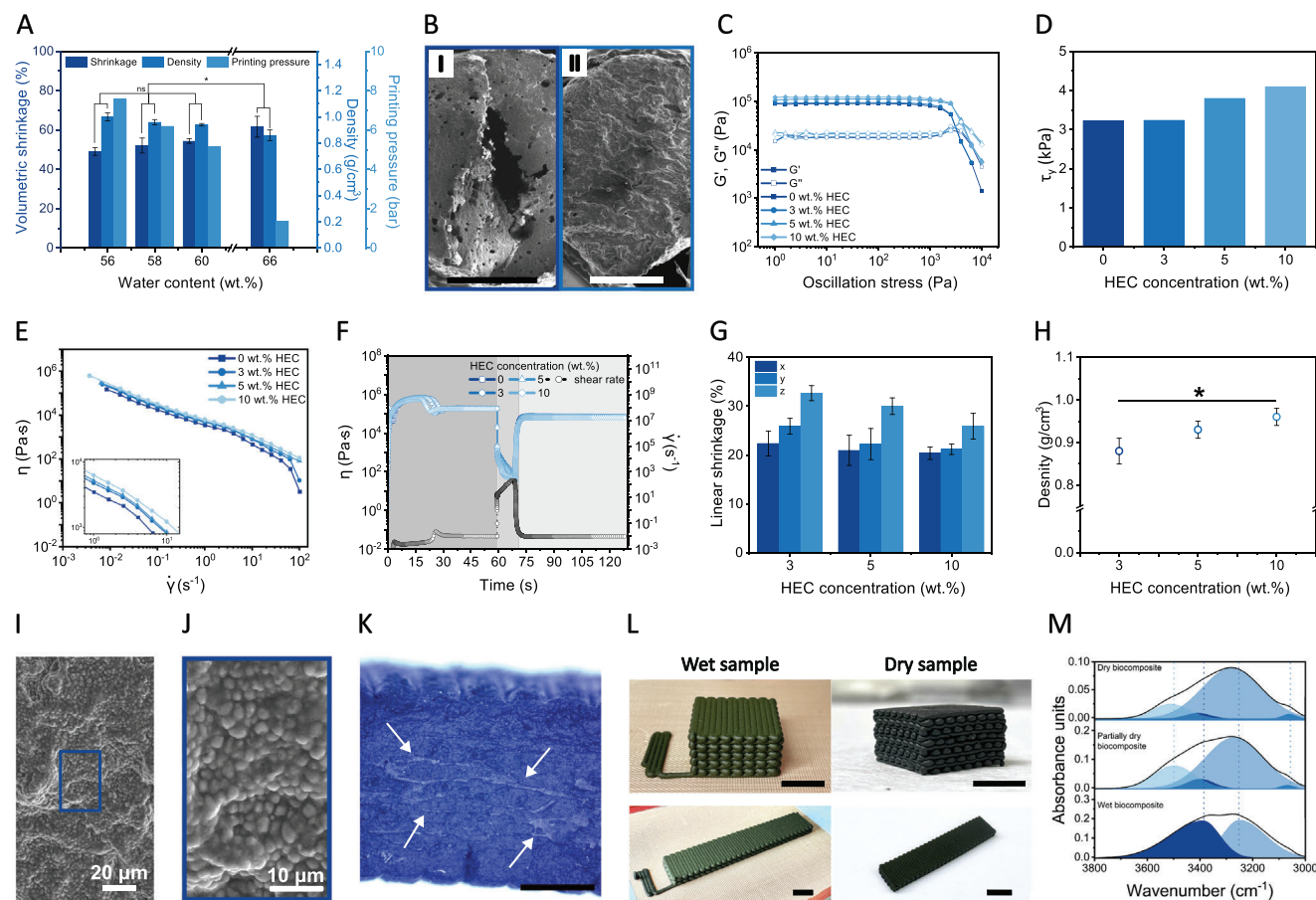
ADVANCED
SCIENCE NEWS

www.advancedsciencenews.com

**ADVANCED
MATERIALS**

www.advmat.de

Figure 2. Printability and hierarchical morphology of the biocomposite. A) Volumetric shrinkage and density variation of the biocomposites after printing and drying, as a function of water concentration in the bioink. B) Binding effect of HEC on the microstructure of *Chlorella* after 3D printing; I) without HEC and II) with 5 wt% HEC; scale bars 500 µm. C,D) Rheological properties of *Chlorella* biocomposites with higher HEC concentration. E) *Chlorella* bioinks have a shear thinning behavior. F) Fast viscosity recovery and shape retention of *Chlorella*–HEC bioinks. G) Linear shrinkage decreases with HEC concentration (*n* = 5). H) The density of the composites increases with HEC concentration (*n* = 5). I–L) Hierarchical structure of biocomposites reinforced with 10 wt% HEC. (I) *Chlorella* cells retain their shape after 3D printing and dehydration. (J) Magnification of the blue area in (I). (K) Morphological control of HEC gels between microalgae layers (pointed with white arrows); scale bar 4 mm. (L) Wet and dry structures with different aspect ratios showing the symmetric printing pattern (0°–90°); scale bars 1 cm. M) Formation of hydrogen bonding in *Chlorella*–HEC composites across different drying states. Group comparisons were performed by one-way Analysis of variance (ANOVA) where ns denotes $p > 0.05$ and * represents $p < 0.05$.

viscosity is likely the result of HEC's physical gelation, resulting from physical interactions, e.g., hydrogen bonding and van der Waals forces, between the HEC macromolecules and water.[44] To ensure the consistency of 3D printed parts, the mass flow rate principle (discussed in Note S1 in the Supporting Information) was applied to adjust the printing speed for every 3D printed sample. This approach ensured that the same amount of material was deposited during extrusion 3D printing, resulting in structures with similar weight, regardless of the different printing parameters (Figure S2d, Supporting Information).

2.2. Shape Integrity of 3D Printed Biocomposites Is Maintained through Bioink Thixotropic Behavior

In particle suspensions, interactions among different cells can significantly affect the rheological behavior of the bioink. High particle concentrations can form a continuous and intercon-

nected network that resists flow, and high shear forces are required to start the flowing process through the printer nozzle. *Chlorella*-based bioink exhibited key characteristics for successful printing: it behaved as a viscoelastic solid ($G' > G''$) at low shear stresses (Figure 2C), had a yield point before flowing (Figure 2C,D), and demonstrated shear-thinning behavior with increased shear rate (Figure 2E). Shear thinning describes how a material's viscosity decreases with increasing shear rate. This behavior plays a crucial role in extrusion-based 3D printing, enabling the material to flow smoothly through the nozzle under high shear forces while maintaining stability and shape upon deposition.[13] Higher concentrations of HEC generated additional gelation sites, promoting cell–gel interactions, and increasing both the shear stress at yield, measured from the G' and G'' crossover during the oscillation test, and viscosity of the bioink (Figure 2C–E). The bioink solvent (water) had a more significant effect on the rheological properties compared to HEC (Figure S4, Supporting Information), as higher water
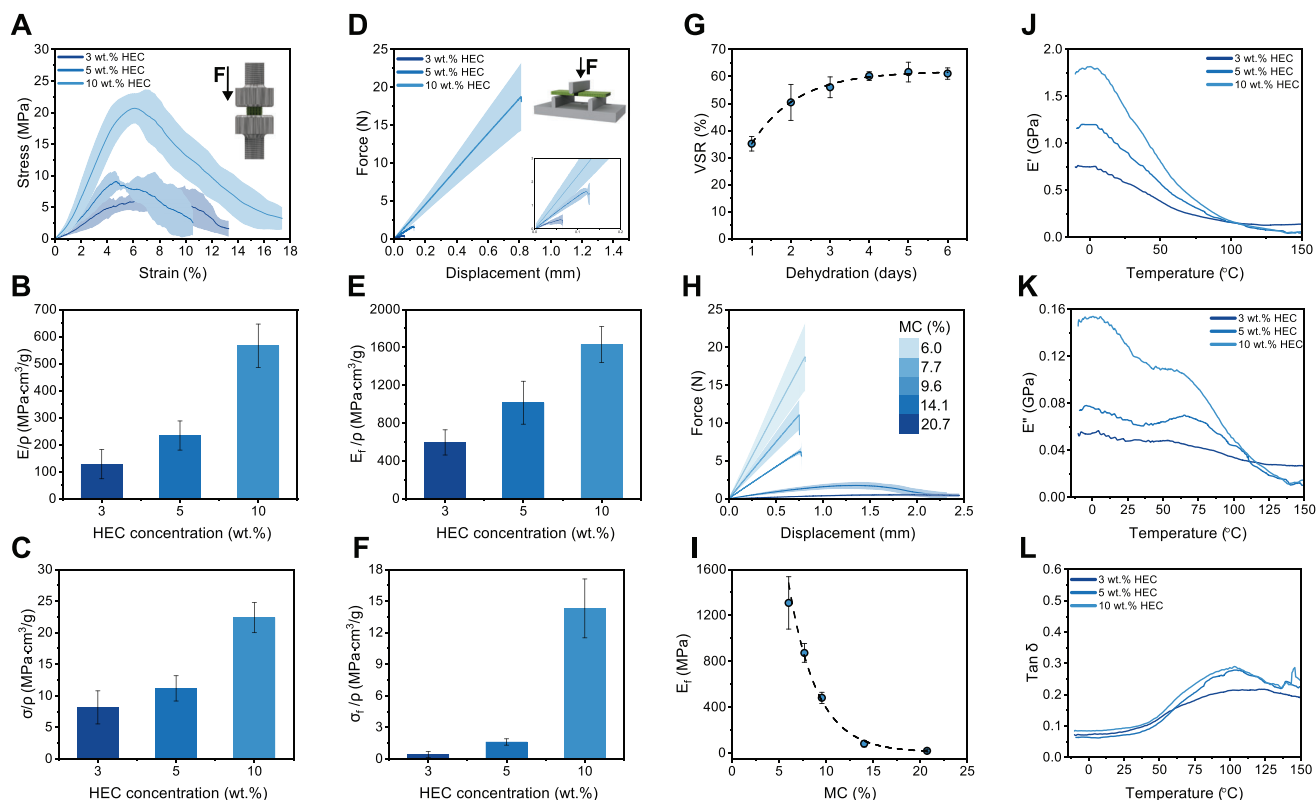
**ADVANCED
SCIENCE NEWS**

www.advancedsciencenews.com

**ADVANCED
MATERIALS**

www.advmat.de

Figure 3. Mechanical characterization of the biocomposites. A) Average stress–strain and D) force–displacement curves under compression and 3-point bending, respectively, of the biocomposites with varying HEC levels ($n = 5$). The modulus and strength of the biocomposite material increases with HEC concentration under B,C) compression and E,F) bending stress. G) The characteristic volumetric shrinkage of the samples at different dehydration times. H) The average force–displacement curves of 10 wt% HEC-reinforced *Chlorella* were measured in 3-point bending as a function of moisture content during the dehydration process ($n = 5$). I) Bending modulus of 10 wt% HEC-reinforced *Chlorella* at different moisture contents corresponding to their respective dehydration time. The J) storage and K) loss moduli of the *Chlorella* biocomposites decrease with temperature. L) tanδ of the *Chlorella* biocomposites as a function of temperature.

concentrations reduced the shear stress at yield and the viscosity of the bioink. This is likely because of the reduction in the overall particle density in the bioink, thus reducing the overall cell–cell interactions.[45] A consistent water concentration of 58 wt% was used for all bioinks from this point. This concentration allowed good printability, moderate volumetric shrinkage, relatively low densities (<1 g cm^{-3}), and faster and controllable dehydration of the printed biocomposite (Figure 2A).

The shear-thinning behavior of *Chlorella* biocomposite inks demonstrated reversible characteristics, with viscosity nearly returning to its original state after shear forces were removed (Figure 2F), demonstrating thixotropic behavior. Under high shear rates, particularly influenced by the conical nozzle geometry, interactions between *Chlorella* particles were disrupted, allowing them to flow independently.[46] After extrusion through the nozzle, when shear forces diminished, cells reorganized and reestablished cell–cell interactions, thereby restoring bioink viscosity and preserving the shape of 3D printed structures.[46] Despite *Chlorella* having a relatively thin cell wall (≈12–14 nm) compared to other microalgae species, its fibrillar morphology and high extracellular polysaccharide content provided sufficient stiffness to maintain the structural integrity of the cell under harsh flow conditions.[37] This resilience was critical as high

shear forces can deform the cells, impacting the rheological properties of the bioink.[47] Deep evaluation of the effect of HEC on the rheological properties of the bioink yielded an optimized 3D printing process, where a continuous and even deposition of biocomposite filaments during fabrication was achieved.

2.3. Slow Dehydration Rates Diminish Differential Shrinkage and Structure Failure after 3D Printing

Dehydration plays an important role in the final mechanical properties of the biocomposites and specifically for *Chlorella*-based materials, it is influenced by the initial water concentration in the bioink. Water concentration affects the volumetric shrinkage and density of the printed materials (as previously described in Section 2.1), along with the bioink printing pressure (Figure 2A). Regardless of the printing parameters used, when samples were dried at ambient conditions, or in an oven at 60 °C, we observed that the morphology of the biocomposites exhibited numerous defects (Figure 2B–I), often leading to catastrophic failure. Consistent with previous studies on bioinks for 3D printing, drying the printed structures under ambient conditions, in an oven, or in a desiccator caused significant shrinkage and
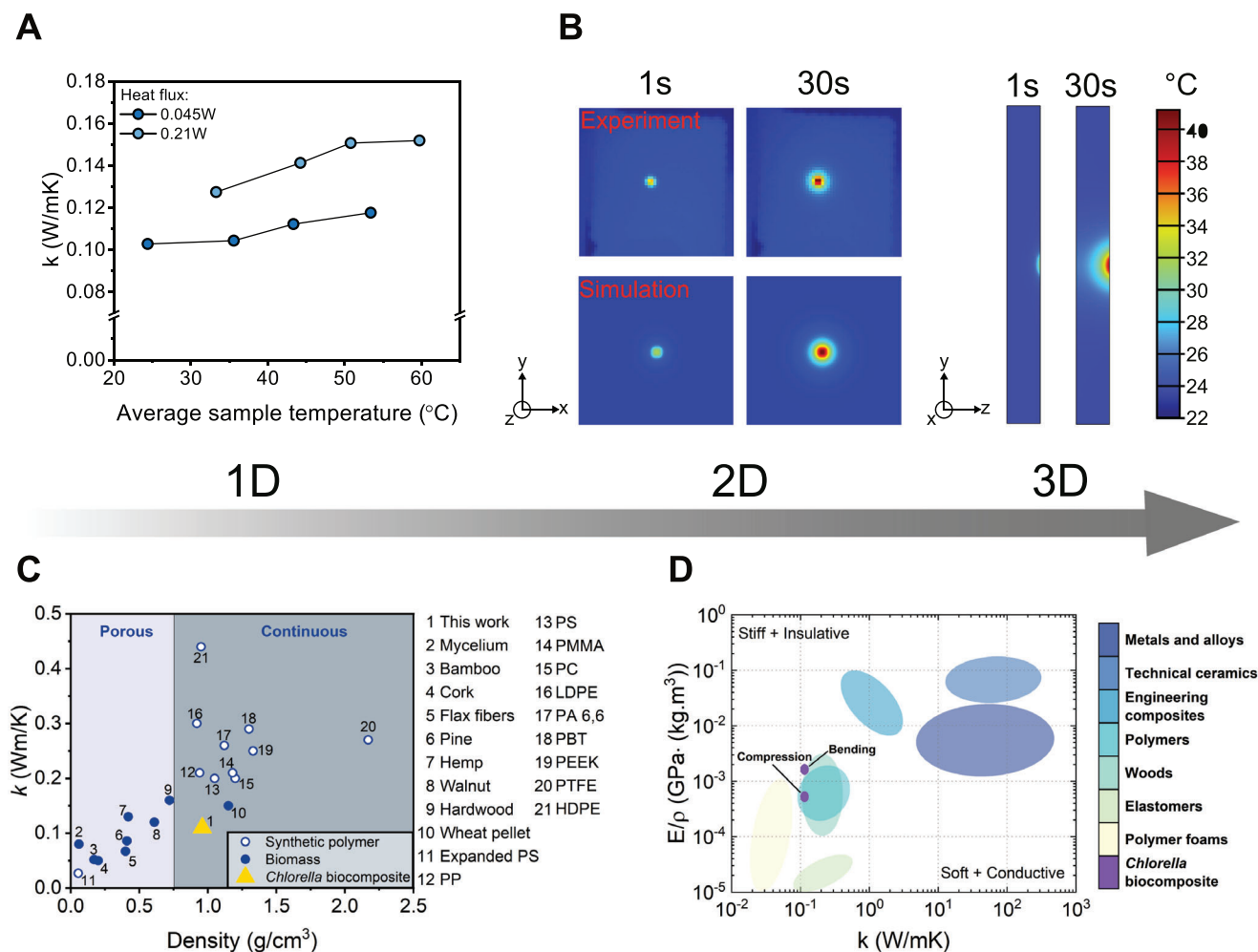
**ADVANCED
SCIENCE NEWS**

www.advancedsciencenews.com

**ADVANCED
MATERIALS**

www.advmat.de

Figure 4. Multidimensional thermal conductivity of *Chlorella* biocomposite. A) Experimental results of 1D thermal conductivity test at different ambient temperatures and heat fluxes. B) Experimental and simulation correlation of the propagation of temperature fields in different time steps after laser emission on the irradiated surface, and simulation of 3D heat flow through the thickness of the biocomposite. C) Comparison of thermal conductivity, as a function of density, of *Chlorella* biocomposite (yellow triangle) and diverse biomass[65,70–73] (blue filled circles) and synthetic polymeric[68,74,75] (white filled circles) materials, with an emphasis on their morphology. D) Normalized Young's modulus versus thermal conductivity for various materials and our biocomposite (in purple) under compression and bending tests, respectively.

microstructural defects, such as cracks, which ultimately led to structural failure.[34,35]

To address this, we developed a controlled, multiphase dehydration protocol (Figure S3a, Supporting Information), inspired by the sol–gel theory of drying[48] (see Note S2 in the Supporting Information). The first stage of drying, known as the constant rate period (CRP), is where most of the structure's shrinkage occurs (Figure 3G), maximizing internal drying stresses. These internal tensile stresses are primarily concentrated near the drying surface, causing differential shrinkage of the structure. When these internal stresses are higher than the strength of the material, cracking and eventually catastrophic failure of the 3D printed part occur. To mitigate differential shrinkage in the 3D printed biocomposite, the CRP needs to be slow.[49] Following 3D printing, the wet structures were placed in an environmental chamber at a relative humidity (RH) of 75% for two days (see the Experimental Section in the Supporting Information). At the beginning, the RH in the chamber increased as water is being rapidly evap-

orated (Figure S3b,c, Supporting Information). After two days, when shrinking stabilized, the samples were moved into a humidity chamber at a RH ≈50% for four days. During this second stage of drying, known as the falling rate period,[48] evaporation occurs at a lower rate, leading to successful, and crack-free, dehydrated 3D printed structures.

2.4. Higher HEC Concentration Reduces Shrinkage and Promotes a Continuous Micromorphology

The HEC concentrations utilized in this study were carefully selected to improve the printing process and ensure the structural integrity of the printed structures. A 3 wt% HEC concentration was determined to be the minimum threshold necessary to produce dehydrated samples without deformation or cracking. Conversely, 10 wt% represented the maximum printable concentration, as higher HEC levels significantly increased viscosity.

**ADVANCED
SCIENCE NEWS**

www.advancedsciencenews.com

**ADVANCED
MATERIALS**

www.advmat.de

Exceeding this concentration resulted in a prolonged 3D printing process using the maximum pressure of our 3D printer, during which the samples began to dry at room temperature, ultimately leading to warping and delamination of the printed layers. It is important to note that, in the absence of HEC, printed structures catastrophically failed during dehydration because of i) the high differential shrinkage developed within the material during the dehydration process; and ii) the absence of binding effect provided by HEC gelation.[48]

To maintain the 3D printed geometry as consistent as possible after printing and dehydration, it is essential to reduce volumetric shrinkage. For biocomposites made with *Chlorella* reinforced with HEC, the in-plane shrinkage is controlled by i) the symmetry of the printing pattern (0°–90°, Figure 2L); and ii) the HEC concentration, whereas the out-of-plan shrinkage is controlled only by the HEC concentration (Figure 2G). Our results show that increasing the HEC concentration from 3 to 10 wt% reduced the linear shrinkage in the x-axis by 9%, in the y-axis by 18%, and in the z-axis by 21%, respectively. These results are consistent with prior work, which reported that increasing the viscosity of the bioink limited the shrinkage and deformation of the printed structures during dehydration.[50]

The density of the biocomposite is also impacted by the HEC concentration (Figure 2H). We observed that an increase in HEC concentration leads to proportionally higher density. Such a behavior has been previously observed in the literature, where increasing the HEC concentration enhanced the density of alumina-based aerogels.[51] Variations in density are correlated to the presence of microstructural defects within the biocomposite, in the form of discontinuities in its microstructure, arising from the binding effect of HEC. At low HEC concentrations, the microstructure of the dehydrated biocomposites presents larger defects, due to the concentration of trapped air within the structure, resulting in low density values (0.87 ± 0.02 g cm^{-3} for 3 wt% HEC). Rising the HEC concentration increased the biocomposite density to 0.93 ± 0.02 g cm^{-3} at 5 wt% HEC and 0.96 ± 0.02 g cm^{-3} for 10 wt% HEC.

HEC binding resulted in a continuous matrix of aggregated cells (Figure 2I,J), leading to a uniform microstructural morphology with a characteristic hierarchical organization. This hierarchical structure is achieved through precise control across multiple scales, from the distribution of bioink components to the final architectural design of the printed material. At the microscale (Figure 2I,J), we carefully manage the distribution and concentration of both *Chlorella* cells and HEC within the bioink, directly influencing the material's properties and structural integrity. This control extends to the millimeter scale, where we optimize the arrangement and interaction of biocomposite layers, where flow-induced HEC interlayer positioning enhances cohesion and consistency throughout the material (Figure 2K). This alternating layer organization significantly impacts mesolevel structure by strengthening interlayer bonds, which is critical for mechanical strength. At the macroscale, we design the overall architecture of the printed structures to align with specific functional goals (Figure 2L). By systematically refining each stage of the fabrication process, we ensure that the controlled hierarchical levels contribute effectively to the biocomposite's overall performance. However, structures with only 3 wt% HEC randomly deformed during drying. This failure emphasizes that lower HEC concentrations are insufficient to effectively bind all biomass, necessitating optimization of HEC content for structural stability.

2.5. Hydrogen Bonding Governs *Chlorella*–HEC Interactions in the Biocomposite

The understanding of hydrogen bonding interactions between *Chlorella* and HEC is crucial for elucidating the mechanisms that govern binding and reinforcement in these biocomposites. Hydrogen bonds formed between the hydroxyl and polar groups of HEC and *Chlorella* are integral to maintaining the mechanical integrity of the biocomposite. Additionally, water in the bioink modulates these interactions by influencing both the strength and density of the hydrogen bonding network throughout dehydration. As the system transitions from a hydrated to a dry state following 3D printing, these interactions evolve, significantly impacting the composite's structure and performance. We used attenuated total reflectance-Fourier transform infrared (ATR-FTIR) spectroscopy to characterize this evolution, focusing on the hydroxyl (—OH) stretching region (3200–3600 cm^{-1}) (Figure 2M). The spectra were deconvoluted to capture delicate changes in bonding interactions. To explore the development of *Chlorella*–HEC interactions within the biocomposite, we evaluated three samples at distinct dehydration stages: i) the wet state, corresponding to the bioink during printing, ii) the semidry state, representing intermediate dehydration, and iii) the dry state, reflecting the fully dehydrated biocomposite.

In the wet state, the deconvoluted spectrum exhibits peaks at 3250 and 3388 cm^{-1} (Figure 2M). These peaks are slightly shifted from the reference O—H stretching peaks of water (3260 cm^{-1}), HEC (3373 cm^{-1}), and *Chlorella* (3273 cm^{-1}) (Figure S5, Supporting Information), suggesting that water-mediated hydrogen bonding plays a dominant role. Water interacts with the hydroxyl groups in both HEC and *Chlorella*, disrupting potential direct interactions between the two components and weakening the overall interfacial bonding.[52] As the system progresses to the semidry state, new peaks emerge at 3068 and 3500 cm^{-1}, with additional shifts to 3269 and 3398 cm^{-1} (Figure 2M). These changes indicate the coexistence of residual water-mediated hydrogen bonds with the onset of direct hydrogen bonding between HEC and *Chlorella*. This transitional phase reflects a progressive displacement of water, enabling the formation of localized hydrogen bonds between the components, which strengthens the interfacial adhesion.[52,53] In the dry state, the spectrum shows peaks at 3060, 3279, 3407, and 3511 cm^{-1} (Figure 2M), marking the dominance of direct hydrogen bonding between HEC and *Chlorella* in the absence of water.[52,54] The shift from the *Chlorella* reference peak at 3273 cm^{-1} (Figure S5, Supporting Information) to 3279 cm^{-1} suggests the formation of enhanced localized interactions, reflecting a stronger, more stable bonding network. This transition aligns with the reduction of water-mediated interactions, which were predominant in earlier phases.

Peaks in the C=O and C—O stretching regions further support this hydrogen bonding evolution (Figure S6, Supporting Information). In the wet state, a peak at 1628 cm^{-1} (between the C=O peaks of water at 1638 cm^{-1} and *Chlorella* at 1623 cm^{-1} (Figure S5, Supporting Information)) suggests water-mediated hydrogen bonding with C=O groups, while peaks at 1538 and

**ADVANCED
SCIENCE NEWS**

www.advancedsciencenews.com

**ADVANCED
MATERIALS**

www.advmat.de

1457 cm^{-1} indicate that water also interacts with amide and C—H groups, further disrupting direct bonding between HEC and *Chlorella*. As the composite becomes semidry, peaks shift to 1737 and 1627 cm^{-1} (Figure S6, Supporting Information), suggesting a gradual displacement of water and the formation of direct hydrogen bonds. In the dry state, peaks at 1739 and 1631 cm^{-1} confirm the dominance of direct hydrogen bonds, with additional shifts in the C—O region further supporting the development of stable, localized interactions (Figure S6, Supporting Information).

These results demonstrate that the hydrogen bonding network within the biocomposite evolves from a hydrated state dominated by water-mediated interactions to a dry state characterized by direct HEC–*Chlorella* bonding, with stronger interactions emerging as water evaporates. The decreasing peak intensity across the states confirms the reduction in hydrogen bond density, with fewer but stronger interactions forming in the absence of water.

2.6. HEC Binding and Reinforcement Enhance Biocomposite's Strength and Stiffness

We first characterized the uniaxial mechanical performance of the biocomposites for different 3D printing parameters (i.e., nozzle diameter and layer height, Figure S7, Supporting Information) and bioink water concentration (Figure S8, Supporting Information). We optimize both the 3D printing process and the bioink formulation to maximize mechanical functionality. We then conducted quasistatic compression and 3-point bending tests (Experimental Section in the Supporting Information) to elucidate the reinforcement effect of HEC on the mechanical behavior of the dehydrated *Chlorella* biocomposites.

Nozzle diameter is an important parameter because it affects both the printing pressure, and the amount of material extruded during the printing process. We study the effect of systematic variations of nozzle diameter, increasing it from 0.84 to 1.6 mm. We observed that the compressive modulus of the biocomposite increased linearly from 80 ± 4 to 96 ± 2 MPa (Figure S7a, Supporting Information). This can be qualitatively explained by the increased layer thickness deposited with larger nozzle diameters, resulting in denser filaments. Smaller nozzle diameters were also investigated; however, the printing time was excessively long, causing the biocomposite to dry during 3D printing, resulting in warping and delamination of the structure. To study the role of layer heights, we fabricated biocomposite structures using a 1.19 mm nozzle diameter increasing the layer height from 0.9 to 1 mm (Figure S7b, Supporting Information). In this small range, we observed an increase in the compression modulus from 78 ± 8 to 115 ± 5 MPa. This increase can be attributed to improved interlayer adhesion and reduced anisotropy of the overall structure, resulting in a denser structure with greater resistance to compressive forces. When layer heights above 1 mm were explored, a decrease in the modulus was observed, likely because of weaker interlayer adhesion and material flow issues.[55] The water concentration influences both the final algae cell concentration in the bioink and the flow and dehydration process. However, the specific modulus (E/ρ) and the specific compressive strength (σ/ρ) of the biocomposites were not affected by changes in water concentration (Figure S8, Supporting Information).

After optimizing 3D printing processing and bioink composition, we turned our attention to understanding the reinforcing effect of HEC (Figure 3). Under uniaxial compression, all stress–strain curves of the biocomposites with different HEC concentrations showed an initial linear regime (Figure 3A). A progressive failure until break was observed after reaching the maximum strength of the materials. An increase of ≈342% for the specific compressive modulus, which was calculated from the initial linear elastic part of the compression experiments (Figure 3B) was observed when increasing the HEC concentration from 3 to 10 wt%. Similarly, the specific strength of the material was enhanced by ≈174% when the HEC concentration raised from 3 to 10 wt% (Figure 3C).

The force–displacement curves of the biocomposites, with different HEC concentrations, under 3-point bending exhibited a linear elastic regime during loading, followed by a catastrophic failure at maximum force, revealing a brittle fracture (Figure 3D). *Chlorella* reinforced with 10 wt% HEC presented a specific bending modulus (E_f/ρ) of 1.7 GPa cm^3 g^{-1}, 173% higher than the bending modulus obtained with a minimal HEC reinforcing concentration of 3 wt% (Figure 3E). Similarly, a maximum specific bending strength (σ_f/ρ) of 14 MPa cm^3 g^{-1} was achieved when reinforcing the *Chlorella* with 10 wt% HEC, while the specific bending strength of the material with 3 wt% HEC was 0.40 MPa cm^3 g^{-1} (Figure 3F). We suggest that the improved mechanical properties of the biocomposite arise from two key mechanisms: i) HEC binding and ii) reinforcing. Higher HEC concentrations reduce defects due to HEC's binding effect, resulting in a uniform microstructure (Figure 2I,J) and increased material density (Figure 2H). Additionally, the dispersion and bonding of HEC molecules to *Chlorella's* cell walls enabled effective stress transfer between the microalgae cells, allowing the biocomposite to resist higher loads (Figure 2M and Figure S6 (Supporting Information)). These mechanisms collectively enhance both the stiffness and strength of the biocomposite. The fracture morphology following the bending test is depicted in the scanning electron microsocpy (SEM) images (Figure 2I,J). Structural analysis was conducted by applying flexural stress to the samples until failure occurred. The SEM images indicate that fracture propagated between *Chlorella* cells rather than through the cells, demonstrating the mechanical resilience and structural robustness of the microalgae.

Our biocomposites exhibited superior mechanical properties compared to those reported for bulk, 3D composite biomaterials designed through bottom-up methods involving eukaryotic organisms, including other microalgae studies,[35] plant cells,[56] mycelium,[57] and yeast matrices.[58] In these biocomposites, microorganism cells function as the essential building blocks of the material, reaching values of 160 and 17 MPa for stiffness and strength, respectively. Nevertheless, it is essential to note that mycelium-based biocomposites have lower densities than our materials.[59]

Analyzing the beam's response to bending loads provides valuable insights into how compression and tensile stresses affect the biocomposite material behavior (Figure S9a, Supporting Information). Using a biocomposite reinforced with 10 wt% HEC as a model material, as a first order approximation, we employed beam theory to calculate the stress distribution of the structure, assuming an isotropic material behavior. The maximum stresses

**ADVANCED
SCIENCE NEWS**

www.advancedsciencenews.com

**ADVANCED
MATERIALS**

www.advmat.de

calculated at the top and bottom surfaces of the beam (compression and tension surfaces, respectively) were ≈15 MPa (Figure S9b, Supporting Information). This stress level falls below the material's maximum compressive strength of 21 MPa, indicating structural integrity under compressive loads (Figure 3C). Conversely, although specific tensile strength data were not measured, the bending test revealed crack initiation from the bottom surface of the beam (Figure S9c, Supporting Information), suggesting potential weakness of *Chlorella* biocomposites under tension.

2.7. Moisture Content Tunes the Stiffness of *Chlorella* Biocomposites, Which Is Limited by the HEC Glass Transition Temperature (T_g)

Moisture and temperature are critical environmental factors that significantly affect the mechanical performance and structural stability of *Chlorella* biocomposites. Elevated moisture levels induce HEC gelation (Figure 2K), leading to a softening of the biocomposite material and a decrease in its stiffness. Moreover, shrinkage can lead to geometric distortions, developing stress concentrations that can result in a weaker structure. Conversely, high temperatures can cause cell wall failure in *Chlorella* and contribute to protein damage within the cell wall structure, potentially compromising the stiffness of the biocomposite.[60] To assess these effects, we conducted 3-point bending tests under various dehydration stages and temperature conditions to analyze how moisture content and temperature variations impact the biocomposite stiffness. Potential weakening effects from cell wall hydration are not considered in the discussion, as the investigation of the hygroscopic properties of dead and alive *Chlorella* cells was not within the scope of this work.

The volumetric shrinkage ratio of the biocomposite, observed over different dehydration periods, shows that the most significant shrinkage occurs within the first two days post-3D printing (Figure 3G), as discussed in Section 2.3 and Note S2 (Supporting Information). During the first stage of dehydration, the CRP, the material undergoes a substantial 50% volume reduction, achieving its final dimensions after 4 days, resulting in an overall volumetric shrinkage of 60%.

We performed 3-point bending tests on biocomposites reinforced with 10 wt% HEC every day during the dehydration process, to understand the effect of internal moisture on the mechanical response (Figure 3H). The structures did not fail catastrophically under bending stress at moisture levels above 14%. Figure 3I demonstrates that reducing moisture content from 21% to 6% consistently increases the stiffness of the biocomposite, from 20 ± 9 to 1310 ± 230 MPa, respectively. This behavior can be attributed to the evolution of hydrogen bonding interactions as moisture content decreases (Figure 2M and Figure S6 (Supporting Information)). In the presence of high humidity, the hydrophilic groups in *Chlorella* cells and HEC, such as —OH groups, preferentially form hydrogen bonds with water molecules, weakening the bonding between adjacent proteins and polysaccharides.[61,62] As water evaporates, the hydrogen bonding network shifts, and direct intermolecular hydrogen bonds between HEC and *Chlorella* components become dominant, significantly enhancing the stiffness and mechanical per-

formance of the composite. This transition aligns with our ATR-FTIR findings (Figure 2M and Figure S6 (Supporting Information)), which reveal that as water content decreases, weaker water-mediated hydrogen bonds are replaced by stronger, localized interactions between the composite's constituents, contributing to the observed increase in stiffness obtained by our analysis.

The effect of temperature on the mechanical properties was studied using dynamic mechanical analysis (DMA) under 3-point bending (Experimental Section in the Supporting Information). Like the results from the quasistatic bending test (Figure 3D,E), the storage modulus (E') and loss modulus (E'') of the *Chlorella*-based biocomposites show increased values with higher HEC concentrations (Figure 3J,K). This indicates that HEC reinforcement enhances both the stiffness and energy dissipation capabilities of the material. After the thermal evolution between 25 and 103 °C, the biocomposite stiffness drops significantly from 1.8 to 0.12 GPa, with 10 wt% HEC reinforcement (Figure 3J), reflecting the behavior of the *Chlorella* cells at high temperatures.[30] The reduction in the loss modulus (Figure 3K) suggests reduced internal friction between the biocomposite components due to the softening of the HEC phase, resulting in less energy being dissipated as heat. The improved energy dissipation is further evidenced by the higher peak in the tanδ values shown in Figure 3L, which indicates a transition from a glassy to a rubbery state at 103 °C.

The T_g of HEC has been reported to be between 106 and 120 °C, depending on the instrument used for measurement.[63,64] The tanδ plot (Figure 3L) suggests that the T_g of HEC in the biocomposite is 103 °C. While T_g is often identified from the peak in the loss modulus (E''), which represents maximum energy dissipation, the peak was not prominent in our analysis (Figure 3K). This could be due to several factors such as the relatively low concentration of HEC within the biocomposite or the interactions between *Chlorella* and HEC, which can affect the sensitivity of the measurement. Despite this, the tanδ peak remains a reliable indicator of T_g as it represents the ratio of the loss modulus to the storage modulus and provides a clear transition point in the viscoelastic behavior of the biocomposite.

2.8. Lightweight *Chlorella* Biocomposites Achieve Isotropic Thermal Insulation and Mechanical Stability

Efficient energy and heat dissipation are characteristic properties of biomass-based materials.[65] *Chlorella* biocomposites are expected to also exhibit good thermal-management capabilities, thanks to their hierarchical structure and biopolymer-based composition.[66] We investigated the thermal insulation capabilities of *Chlorella* biocomposites and their resistance to heat flow, measuring the 1D thermal conductivity using a steady-state method (Figure S10a, Supporting Information). Subsequently, we employed a modified laser-flash method to irradiate the biocomposite surface and explore heat flow behavior in 2D at room temperature (Figure S10b, Supporting Information). Finally, we conducted a 3D simulation to analyze the heat flow behavior. The experiments were performed on samples with a continuous morphology, specifically *Chlorella* reinforced with 10 wt% HEC.

The thermal conductivity (k) of *Chlorella* biocomposites increases with temperature (Figure 4a). This trend is consistent across different heat fluxes and aligns with the thermal conductivity behavior of bulk polymers.[67] Under extreme conditions at −26.1 °C, the thermal conductivity values were 0.075 and 0.095 W mK^{-1} for heat fluxes of 0.045 and 0.21 W, respectively. When the temperature was increased to room temperature and then continuously to 50 °C, the thermal conductivity for a heat flux of 0.045 W increased from 0.103 to 0.118 W mK^{-1}. For a higher heat flux of 0.21 W, the thermal conductivity of the *Chlorella* biocomposite increased to 0.127 W mK^{-1} at room temperature and reached 0.152 W mK^{-1} at 50 °C.

Figure 4B and Figure S13 (Supporting Information) illustrate the temporal evolution of field temperatures on the irradiated and opposite surfaces of the biocomposite, respectively, showing the nature of 2D heat flow in the sample. These field temperature maps reveal uniform heat dissipation in all directions, consistent with the temperature profiles over time shown in Figure S12a (Supporting Information). At 30 s, the irradiated surface reached a maximum temperature of 41.3 °C, while the opposite surface registered 26.4 °C. To analyze heat propagation across the sample thickness, we correlated temperature profiles (Figure S12, Supporting Information) and field temperatures (Figure 4B and Figure S13 (Supporting Information)) with a 3D model. The agreement between experimental 2D results and 3D model was validated using thermal conductivity data from steady-state experiments and heat capacity calculations from modulated differential scanning calorimetry (Figure S14, Supporting Information), all of which demonstrated the sample's heat conduction to be isotropic in nature. The resulting 3D temperature fields illustrate isotropic heat flow over different time intervals.

Thermal conductivity in polymeric materials is influenced by several factors such as crystallinity, processing conditions, morphology, defects, and thermal anisotropy.[68] The heat transfer of *Chlorella* was not affected by the infill pattern from the 3D printing process, as is often observed in 3D printed bulk polymers and their composites.[69] Bulk polymers, characterized by high molecular weight and random entanglements with low degrees of crystallinity and large free volumes, typically exhibit thermal insulation properties as a result of phonon scattering. By contrast, the *Chlorella* biocomposite developed in this study demonstrates superior insulation compared to bulk polymers, partly due to its low density of 0.96 g cm^{-3}. To illustrate this, thermal conductivity at room temperature was plotted against density for various bulk polymers and biomass-based materials (Figure 4C). Biomass-based materials, like wood and lignocellulosic fibers, with densities up to 0.75 g cm^{-3}, benefit from their porous structure, resulting in thermal conductivity values below 0.1 W mK^{-1}. Conversely, materials with continuous morphologies and higher densities (>1 g cm^{-3}), such as high-density polyethylene with a thermal conductivity up to 0.45 W mK^{-1}, exhibit higher thermal conductivity values by improving phonon transport and reduced air–material interfaces.

Wood materials often enhance thermal insulation through delignification, which not only removes lignin but also introduces nanopores within cell walls.[66] This process reduces phonon transport while enhancing anisotropic thermal conductivity due to improved alignment of cellulose nanofibrils. In contrast to wood and natural fibers, *Chlorella* microalgae lack the presence of lignin within the cell composition.[38] Moreover, *Chlorella* biocomposites demonstrate isotropic heat transfer while maintaining a continuous morphology, offering mechanical properties comparable to both bulk polymers and wood, alongside effective thermal insulation (Figure 4D).

3. Conclusion

We developed hierarchical biocomposite materials based on *Chlorella* algae, fabricated through extrusion 3D printing at room temperature, without the use of any petrochemical-based additives. Our study demonstrates that *Chlorella*-based bioinks can withstand the high shear forces involved in 3D printing, preserving the integrity of the cells and ensuring continuous morphologies post-processing. The rapid viscosity recovery mechanism enables the biocomposites to maintain their shape immediately after printing. A practical dehydration protocol was implemented, preventing cracking and yielding biocomposites with stable morphologies of aggregated cells. ATR-FTIR analysis revealed that hydrogen bonding plays a key role in the mechanical reinforcement of the biocomposites. As the water content decreases, the system transitions from water-mediated hydrogen bonding to direct hydrogen bonds between hydroxyl groups in HEC and *Chlorella* cells. This shift strengthens the interactions between the two components, contributing to the improved compression and bending moduli observed in the dry biocomposites (566 and 1630 MPa, respectively). The presence of water enhances the rheological properties of the bioink, facilitating optimal printability without compromising mechanical performance.

Our method maximizes the structural capabilities of the biocomposite, with HEC acting as both a binder and reinforcement. Thermal conductivity tests demonstrated isotropic heat transfer with a low thermal conductivity of 0.10 W mK^{-1}, making the material effective as a thermal insulator. The approach presented here is adaptable to other microalgae strains with varied cell shapes and sizes, potentially enabling sustainable material production for diverse applications.

Further extensions of this research could explore 1) the fracture toughness and impact resistance of the biocomposites, 2) the effect of post-printing treatments (e.g., annealing) on morphology and mechanical properties, 3) the incorporation of natural fibers to enhance stiffness and thermal insulation, and 4) the scalability of fabricating complex 3D structures. These *Chlorella* biocomposites show great potential as substitutes for bulk polymers and wood in applications requiring both, high mechanical strength and thermal insulation, including construction, packaging, and furniture.

Supporting Information

Supporting Information is available from the Wiley Online Library or from the author.

Acknowledgements

**ADVANCED
SCIENCE NEWS**

www.advancedsciencenews.com

**ADVANCED
MATERIALS**

www.advmat.de

Conflict of Interest

The authors declare no conflict of interest.

Data Availability Statement

The data that support the findings of this study are available from the corresponding author upon reasonable request.

Keywords

[1] J. A. Lewis, *Adv. Funct. Mater.* **2006**, *16*, 2193.
[2] S. Ghosh, S. T. Parker, X. Wang, D. L. Kaplan, J. A. Lewis, *Adv. Funct. Mater.* **2008**, *18*, 1883.
[3] R. J. Kadakia, C. M. Wixted, N. B. Allen, A. E. Hanselman, S. B. Adams, *3D Print. Med.* **2020**, *6*, 29.
[4] C.-Y. Liaw, M. Guvendiren, *Biofabrication* **2017**, *9*, 024102.
[5] A. Le Duigou, A. Barbé, E. Guillou, M. Castro, *Mater. Des.* **2019**, *180*, 107884.
[6] C. Aumnate, N. Soatthiyanon, T. Makmoon, P. Potiyaraj, *Cellulose* **2021**, *28*, 8509.
[7] T. Li, J. Chang, Y. Zhu, C. Wu, *Adv. Healthcare Mater.* **2020**, *9*, 2000208.
[8] H. Martínez Ávila, S. Schwarz, N. Rotter, P. Gatenholm, *Bioprinting* **2016**, *1–2*, 22.
[9] S. Zhao, C. Guo, A. Kumarasena, F. G. Omenetto, D. L. Kaplan, *ACS Biomater. Sci. Eng.* **2019**, *5*, 4808.
[10] J. J. Oh, S. Ammu, V. D. Vriend, R. Kieffer, F. H. Kleiner, S. Balasubramanian, E. Karana, K. Masania, M. E. Aubin-Tam, *Adv. Mater.* **2024**, *36*, 2305505.
[11] M. Müller, P. Fisch, M. Molnar, S. Eggert, M. Binelli, K. Maniura-Weber, M. Zenobi-Wong, *Mater. Sci. Eng., C* **2020**, *108*, 110510.
[12] M. A. Skylar-Scott, S. G. M. Uzel, L. L. Nam, J. H. Ahrens, R. L. Truby, S. Damaraju, J. A. Lewis, *Sci. Adv.* **2019**, *5*, eaaw2459.
[13] J. Wang, Y. Liu, X. Zhang, S. E. Rahman, S. Su, J. Wei, F. Ning, Z. Hu, R. Martínez-Zaguilán, S. R. Sennoune, W. Cong, G. Christopher, K. Zhang, J. Qiu, *Polymer* **2021**, *214*, 123238.
[14] A. Lueckgen, D. S. Garske, A. Ellinghaus, D. J. Mooney, G. N. Duda, A. Cipitria, *Acta Biomater.* **2020**, *115*, 185.
[15] B. Zhang, L. Wang, P. Song, X. Pei, H. Sun, L. Wu, C. Zhou, K. Wang, Y. Fan, X. Zhang, *Mater. Des.* **2021**, *201*, 109490.
[16] N. Rezania, M. Asadi-Eydivand, N. Abolfathi, S. Bonakdar, M. Mehrjoo, M. Solati-Hashjin, *J. Mater. Sci.: Mater. Med.* **2022**, *33*, 31.
[17] C. Vyas, J. Zhang, Ø. Øvrebø, B. Huang, I. Roberts, M. Setty, B. Allardyce, H. Haugen, R. Rajkhowa, P. Bartolo, *Mater. Sci. Eng., C* **2021**, *118*, 111443.
[18] S. A. Hinchcliffe, K. M. Hess, W. V. Srubar, *Composites, Part B* **2016**, *95*, 346.
[19] A. Le Duigou, M. Castro, R. Bevan, N. Martin, *Mater. Des.* **2016**, *96*, 106.
[20] I. Kellersztein, A. Dotan, *Polym. Compos.* **2016**, *37*, 2133.
[21] W. Sun, M. Tajvidi, C. G. Hunt, G. McIntyre, D. J. Gardner, *Sci. Rep.* **2019**, *9*, 3766.
[22] J. Song, C. Chen, S. Zhu, M. Zhu, J. Dai, U. Ray, Y. Li, Y. Kuang, Y. Li, N. Quispe, Y. Yao, A. Gong, U. H. Leiste, H. A. Bruck, J. Y. Zhu, A. Vellore, H. Li, M. L. Minus, Z. Jia, A. Martini, T. Li, L. Hu, *Nature* **2018**, *554*, 224.
[23] C. Y. B. Oliveira, C. D. L. Oliveira, R. Prasad, H. C. Ong, E. S. Araujo, N. Shabnam, A. O. Gálvez, *Rev. Aquacult.* **2021**, *13*, 1594.
[24] Z. L. Lau, S. S. Low, E. R. Ezeigwe, K. W. Chew, W. S. Chai, A. Bhatnagar, Y. J. Yap, P. L. Show, *Bioresour. Technol.* **2022**, *351*, 127048.
[25] K. S. Khoo, Y. M. Chong, W. S. Chang, J. M. Yap, S. C. Foo, I. Khoiroh, P. L. Lau, K. W. Chew, C. W. Ooi, P. L. Show, *Sep. Purif. Technol.* **2021**, *256*, 117471.
[26] S. O. Cinar, Z. K. Chong, M. A. Kucuker, N. Wieczorek, U. Cengiz, K. Kuchta, *Int. J. Environ. Res. Public Health* **2020**, *17*, 3842.
[27] C. Zhang, P.-L. Show, S.-H. Ho, *Bioresour. Technol.* **2019**, *289*, 121700.
[28] V. V. Devadas, K. S. Khoo, W. Y. Chia, K. W. Chew, H. S. H. Munawaroh, M. K. Lam, J. W. Lim, Y. C. Ho, K. T. Lee, P. L. Show, *Bioresour. Technol.* **2021**, *325*, 124702.
[29] A. Nakanishi, K. Iritani, Y. Sakihama, M. Watanabe, *Int. J. Microbiol. Biotechnol.* **2020**, *5*, 159.
[30] M. A. Zeller, R. Hunt, A. Jones, S. Sharma, *J. Appl. Polym. Sci.* **2013**, *130*, 3263.
[31] M. Bulota, T. Budtova, *Composites, Part A* **2015**, *73*, 109.
[32] N. Zhu, M. Ye, D. Shi, M. Chen, *Macromol. Res.* **2017**, *25*, 165.
[33] M. Y. Lin, P. Grandgeorge, A. M. Jimenez, B. H. Nguyen, E. Roumeli, *ACS Sustainable Chem. Eng.* **2023**, *11*, 8242.
[34] C. Kwak, S. Young Ryu, H. Park, S. Lim, J. Yang, J. Kim, J. Hyung Kim, J. Lee, *J. Colloid Interface Sci.* **2021**, *582*, 81.
[35] J. L. Fredricks, H. Iyer, R. McDonald, J. Hsu, A. M. Jimenez, E. Roumeli, *J. Polym. Sci.* **2021**, *59*, 2878.
[36] B. G. Compton, J. A. Lewis, *Adv. Mater.* **2014**, *26*, 5930.
[37] K. Jothibasu, I. Muniraj, T. Jayakumar, B. Ray, D. W. Dhar, S. Karthikeyan, S. Rakesh, *Biochem. Eng. J.* **2022**, *187*, 108642.
[38] C. Safi, B. Zebib, O. Merah, P. Y. Pontalier, C. Vaca-Garcia, *Renewable Sustainable Energy Rev.* **2014**, *35*, 265.
[39] L. Dai, T. Cheng, C. Duan, W. Zhao, W. Zhang, X. Zou, J. Aspler, Y. Ni, *Carbohydr. Polym.* **2019**, *203*, 71.
[40] Y. Song, Q. Zheng, C. Liu, *Ind. Crops Prod.* **2008**, *28*, 56.
[41] B. Saša, P. Odon, S. Stane, K. Julijana, *Eur. J. Pharm. Sci.* **2006**, *27*, 375.
[42] D. Sinha Roy, B. D. Rohera, *Eur. J. Pharm. Sci.* **2002**, *16*, 193.
[43] X. Li, Q. Deng, S. Wang, Q. Li, W. Zhao, B. Lin, Y. Luo, X. Zhang, *3D Print. Addit. Manuf.* **2021**, *8*, 87.
[44] T. Gong, Y. Hou, X. Yang, Y. Guo, *Int. J. Biol. Macromol.* **2019**, *134*, 547.
[45] S. B. El Attar, A. Morillas-España, J. L. C. López, M. G. Pinna-Hernández, G. Acién, *New Biotechnol.* **2022**, *72*, 107.
[46] S. Xin, K. A. Deo, J. Dai, N. Krishna Rajeeva Pandian, D. Chimene, R. M. Moebius, A. Jain, A. Han, A. K. Gaharwar, D. L. Alge, *Sci. Adv.* **2021**, *7*, eabk3087.
[47] J. A. Espina, M. H. Cordeiro, M. Milivojevic, I. Pajić-Lijaković, E. H. Barriga, *J. Cell Sci.* **2023**, *136*, 260985.
[48] G. W. Scherer, *J. Am. Ceram. Soc.* **1990**, *73*, 3.
[49] I. Jayawardena, P. Turunen, B. C. Garms, A. Rowan, S. Corrie, L. Grøndahl, *Mater. Adv.* **2023**, *4*, 669.
[50] Y. Shao, D. Chaussy, P. Grosseau, D. Beneventi, *Ind. Eng. Chem. Res.* **2015**, *54*, 10575.

[51] C. Simón-Herrero, A. Romero, J. L. Valverde, L. Sánchez-Silva, *J. Mater. Sci.* **2018**, *53*, 1556.

[52] D. Zhao, A. Sultana, J. Edberg, M. Shiran Chaharsoughi, M. Elmahmoudy, U. Ail, K. Tybrandt, X. Crispin, *J. Mater. Chem. C* **2022**, *10*, 2732.

[53] D. Yue, H. Zhang, M. Liu, B. Li, Y. Ge, D. Sun, F. Li, *Polymer* **2022**, *254*, 125048.

[54] N. Arfin, H. B. Bohidar, *Int. J. Biol. Macromol.* **2012**, *50*, 759.

[55] J. Brackett, D. Cauthen, J. Condon, T. Smith, N. Gallego, V. Kunc, C. Duty, *Addit. Manuf.* **2022**, *58*, 103063.

[56] L. Valentini, S. B. Bon, S. Signetti, M. Tripathi, E. Iacob, N. M. Pugno, *Sci. Rep.* **2016**, *6*, 27031.

[57] L. Peng, J. Yi, X. Yang, J. Xie, C. Chen, *J. Bioresour. Bioprod.* **2023**, *8*, 78.

[58] L. Valentini, S. Bittolo Bon, S. Signetti, N. M. Pugno, *ACS Appl. Mater. Interfaces* **2016**, *8*, 7607.

[59] E. Soh, Z. Y. Chew, N. Saeidi, A. Javadian, D. Hebel, H. L. Ferrand, *Mater. Des.* **2020**, *195*, 109058.

[60] M. Šoštarič, D. Klinar, M. Bricelj, J. Golob, M. Berovič, B. Likozar, *New Biotechnol.* **2012**, *29*, 325.

[61] I. Kellersztein, I. Greenfeld, H. D. Wagner, *Bioinspir. Biomim.* **2021**, *16*, 026013.

[62] A. Rosenberg, A. Solomonov, H. Cohen, D. Eliaz, I. Kellersztein, O. Brookstein, A. Kozell, L. Wang, H. D. Wagner, C. Daraio, U. Shimanovich, *ACS Appl. Mater. Interfaces* **2024**, *16*, 9210.

[63] T. T. Kararli, J. B. Hurlbut, T. E. Needham, *J. Pharm. Sci.* **1990**, *79*, 845.

[64] E. Doelker, in *Absorbent Polymer Technology* (Eds: L. Brannon-Peppas, R. S. Harland), Elsevier Science Publishers B. V, New York **1990**, pp. 125–146.

[65] L. Long, H. Ye, *Sci. Rep.* **2016**, *6*, 24181.

[66] C. Chen, Y. Kuang, S. Zhu, I. Burgert, T. Keplinger, A. Gong, T. Li, L. Berglund, S. J. Eichhorn, L. Hu, *Nat. Rev. Mater.* **2020**, *5*, 642.

[67] W. N. Dos Santos, J. A. De Sousa, R. Gregorio, *Polym. Test.* **2013**, *32*, 987.

[68] Y. Guo, K. Ruan, X. Shi, X. Yang, J. Gu, *Compos. Sci. Technol.* **2020**, *193*, 108134.

[69] H. Guo, H. Zhao, H. Niu, Y. Ren, H. Fang, X. Fang, R. Lv, M. Maqbool, S. Bai, *ACS Nano* **2021**, *15*, 6917.

[70] I. Hamrouni, H. Jalili, T. Ouahbi, S. Taibi, M. Jamei, A. Mabrouk, *Constr. Build. Mater.* **2024**, *423*, 135828.

[71] Z. Huang, Y. Sun, F. Musso, *Constr. Build. Mater.* **2018**, *177*, 342.

[72] A. D'Alessandro, C. Fabiani, A. L. Pisello, F. Ubertini, A. Luigi Materazzi, F. Cotana, *Int. J. Low-Carbon Technol.* **2017**, *12*, 289.

[73] M. Zhang, J. Xue, R. Zhang, W. Zhang, Y. Peng, M. Wang, J. Cao, *Small* **2023**, *19*, 2302827.

[74] J. R. Zhao, R. Zheng, J. Tang, H. J. Sun, J. Wang, *J. Hazard. Mater.* **2022**, *438*, 129449.

[75] Y. Yuan, Z. Li, L. Cao, B. Tang, S. Zhang, *Ceram. Int.* **2019**, *45*, 16569.